Corrections

EARTH, ATMOSPHERIC, AND PLANETARY SCIENCES

Correction for "High-precision timeline for Earth's most severe extinction," by Seth D. Burgess, Samuel Bowring, and Shu-zhong Shen, which appeared in issue 9, March 4, 2014, of *Proc Natl Acad Sci USA* (111:3316–3321; first published February 10, 2014; 10.1073/pnas.1317692111).

The authors note that Fig. 3 and its corresponding legend appeared incorrectly. The corrected figure and legend appear below.

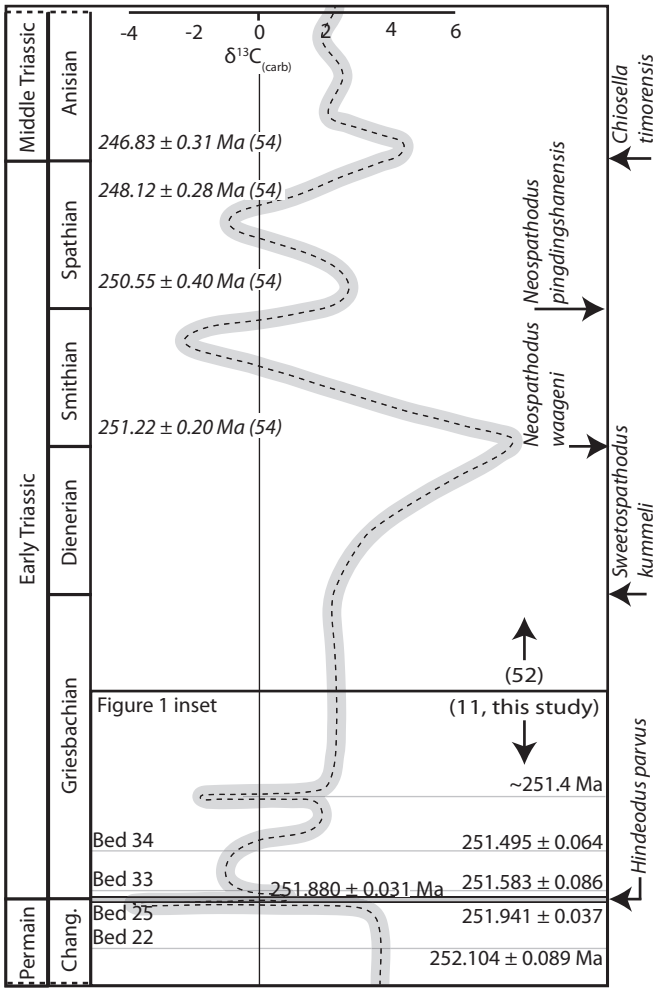

Fig. 3. Generalized Changshingian to Anisian carbonate carbon isotopic composition from South China. Bed thickness and number, carbonate carbon isotopic composition, weighted mean $^{206}Pb/^{238}U$ dates, and extinction interval (gray) within Fig. 1, *Inset* from this study and Cao et al. (11). Remainder of carbonate carbon isotopic composition from Payne et al. (52) and geochronology from Galfetti et al. (54). Permian and Triassic conodont zones from Ogg et al. (63). Stage/substage names are global standard chronostratigraphic units used by the International Commission on Stratigraphy.

www.pnas.org/cgi/doi/10.1073/pnas.1403228111

BIOPHYSICS AND COMPUTATIONAL BIOLOGY

Correction for "Trends in structural coverage of the protein universe and the impact of the Protein Structure Initiative," by Kamil Khafizov, Carlos Madrid-Aliste, Steven C. Almo, and Andras Fiser, which appeared in issue 10, March 11, 2014, of *Proc Natl Acad Sci USA* (111:3733–3738; first published February 24, 2014; 10.1073/pnas.1321614111).

The authors note that the following statement should be added as a new Acknowledgments section: "This work was supported by grants from the National Institutes of Health (GM094665, GM094662, GM096041)."

www.pnas.org/cgi/doi/10.1073/pnas.1404196111

IMMUNOLOGY

Correction for "Vaccine-elicited primate antibodies use a distinct approach to the HIV-1 primary receptor binding site informing vaccine redesign," by Karen Tran, Christian Poulsen, Javier Guenaga, Natalia de Val Alda, Richard Wilson, Christopher Sundling, Yuxing Li, Robyn L. Stanfield, Ian A. Wilson, Andrew B. Ward, Gunilla B. Karlsson Hedestam, and Richard T. Wyatt, which appeared in issue 7, February 18, 2014, of *Proc Natl Acad Sci USA* (111:E738–E747; first published February 3, 2014; 10.1073/pnas.1319512111).

The authors note that the author name Natalia de Val Alda should instead appear as Natalia de Val. The corrected author line appears below. The online version has been corrected.

Karen Tran, Christian Poulsen, Javier Guenaga, Natalia de Val, Richard Wilson, Christopher Sundling, Yuxing Li, Robyn L. Stanfield, Ian A. Wilson, Andrew B. Ward, Gunilla B. Karlsson Hedestam, and Richard T. Wyatt

www.pnas.org/cgi/doi/10.1073/pnas.1403776111

High-precision timeline for Earth's most severe extinction

Seth D. Burgess[a,1], Samuel Bowring[a], and Shu-zhong Shen[b]

[a]Department of Earth, Atmospheric, and Planetary Sciences, Massachusetts Institute of Technology, Cambridge, MA 02139; and [b]State Key Laboratory of Palaeobiology and Stratigraphy, Nanjing Institute of Geology and Palaeontology, Chinese Academy of Sciences, Nanjing, Jiangsu 210008, People's Republic of China

Edited by Dennis Kent, Rutgers University and Lamont-Doherty Earth Observatory, Palisades, NY, and approved January 2, 2014 (received for review September 18, 2013)

The end-Permian mass extinction was the most severe loss of marine and terrestrial biota in the last 542 My. Understanding its cause and the controls on extinction/recovery dynamics depends on an accurate and precise age model. U-Pb zircon dates for five volcanic ash beds from the Global Stratotype Section and Point for the Permian-Triassic boundary at Meishan, China, define an age model for the extinction and allow exploration of the links between global environmental perturbation, carbon cycle disruption, mass extinction, and recovery at millennial timescales. The extinction occurred between 251.941 ± 0.037 and 251.880 ± 0.031 Mya, an interval of 60 ± 48 ka. Onset of a major reorganization of the carbon cycle immediately precedes the initiation of extinction and is punctuated by a sharp (3‰), short-lived negative spike in the isotopic composition of carbonate carbon. Carbon cycle volatility persists for ∼500 ka before a return to near preextinction values. Decamillenial to millennial level resolution of the mass extinction and its aftermath will permit a refined evaluation of the relative roles of rate-dependent processes contributing to the extinction, allowing insight into post-extinction ecosystem expansion, and establish an accurate time point for evaluating the plausibility of trigger and kill mechanisms.

geochronology | evolution

The ability to examine the rock record at millennial to decamillennial time scales in rocks that are hundreds of millions of years old permits critical evaluation of the patterns and rates of climate change, biological response to environmental perturbations, and evolution in deep time. This knowledge can give context to our understanding of the scale and rate of current biologic and climate change. In this article, we show that the largest known extinction in the history of animal life occurred in tens of thousands of years, just after a short-lived and major reorganization of the global carbon cycle.

Mass extinctions have long garnered attention, as they are characterized by fundamental restructuring of marine and terrestrial ecosystems and reflect complex feedbacks between environmental change, extinction, and recovery. However, it is only rarely that environmental perturbation leads to global extinction. Proposed drivers of mass extinctions range from asteroid impact to flood basalt volcanism, which are thought to trigger kill mechanisms ranging from global ocean anoxia to high atmospheric pCO_2 to high ocean and atmosphere temperatures, for example (1). Although the geologic record is replete with occurrences of all of these, very few lead to mass extinctions. Studying the temporal details of mass extinctions is crucial for understanding how they are triggered and may allow isolation and identification of processes that are associated with a characteristic timescale. These processes in turn may be relevant to current biological and climate change and the timescales of feedbacks between environmental change and extinction.

The last two decades have seen a great deal of interest in the largest Phanerozoic extinction, the end-Permian biotic crisis, and an increased understanding of the patterns and timing of extinction and recovery, the synchronous and rapid perturbation of the global ocean-atmosphere system, and plausible trigger(s) and kill mechanisms (1–6). Attempts to reconcile the patterns and rates of extinction in marine and terrestrial environments has led to some agreement on the nature of severe environmental changes, including increased atmospheric pCO_2 and acidification of the oceans, as well as widespread euxinic/anoxic conditions and a sharp spike in sea surface temperature (4, 7–12), and inferentially, kill mechanism(s).

Since 1998, four major U-Pb geochronological studies have attempted to constrain the timing and duration of the extinction (3, 13–15). To better understand the relationship between environmental perturbation and biotic response, accurate and precise age models that integrate geochronology, paleontology, and geochemistry must be developed (8, 11, 16, 17). Recognition of astronomically forced sedimentary cycles (Milankovitch cycles) in late Permian and Triassic sedimentary rocks tuned with available geochronology have been used to refine existing age models of the biotic crisis (18–20). Published estimates of the extinction interval based on radioisotopic dates range from ∼1.5 Mya to approximately <200 ± 100 ka, whereas astrochronological interpretations range from ∼700 ka to as little as ∼10 ka (3, 14, 15, 18, 19). Most recently, Wu et al. (20) used Milankovitch cyclicity and previously published geochronology to constrain the maximum extinction interval at Meishan to 83 ka. Published geochronology is not sufficiently precise to test this estimate.

The geology, biostratigraphy, and chemostratigrahy of the Global Stratotype Section and Point (GSSP) for the Permian-Triassic boundary at Meishan, China, have been previously described in detail (3, 11, 21, 22), and the section contains volcanic ash beds interlayered with fossil-bearing carbonate rocks (Fig. 1 and Fig. S1). In this article, we use the significant progress made in U-Pb geochronology since the acquisition of the data

Significance

Mass extinctions are major drivers of macroevolutionary change and mark fundamental transitions in the history of life, yet the feedbacks between environmental perturbation and biological response, which occur on submillennial timescales, are poorly understood. We present a high-precision age model for the end-Permian mass extinction, which was the most severe loss of marine and terrestrial biota in the last 542 My, that allows exploration of the sequence of events at millennial to decamillenial timescales 252 Mya. This record is critical for a better understanding of the punctuated nature and duration of the extinction, the reorganization of the carbon cycle, and a refined evaluation of potential trigger and kill mechanisms.

Author contributions: S.D.B. performed research; S.B. and S.-z.S. collected samples; S.D.B. did the isotopic analyses; S.B. and S.-z.S. contributed to writing and data interpretation; and S.D.B. wrote the paper.

The authors declare no conflict of interest.

This article is a PNAS Direct Submission.

See Commentary on page 3203.

[1]To whom correspondence should be addressed. E-mail: sburgess@mit.edu.

This article contains supporting information online at www.pnas.org/lookup/suppl/doi:10.1073/pnas.1317692111/-/DCSupplemental.

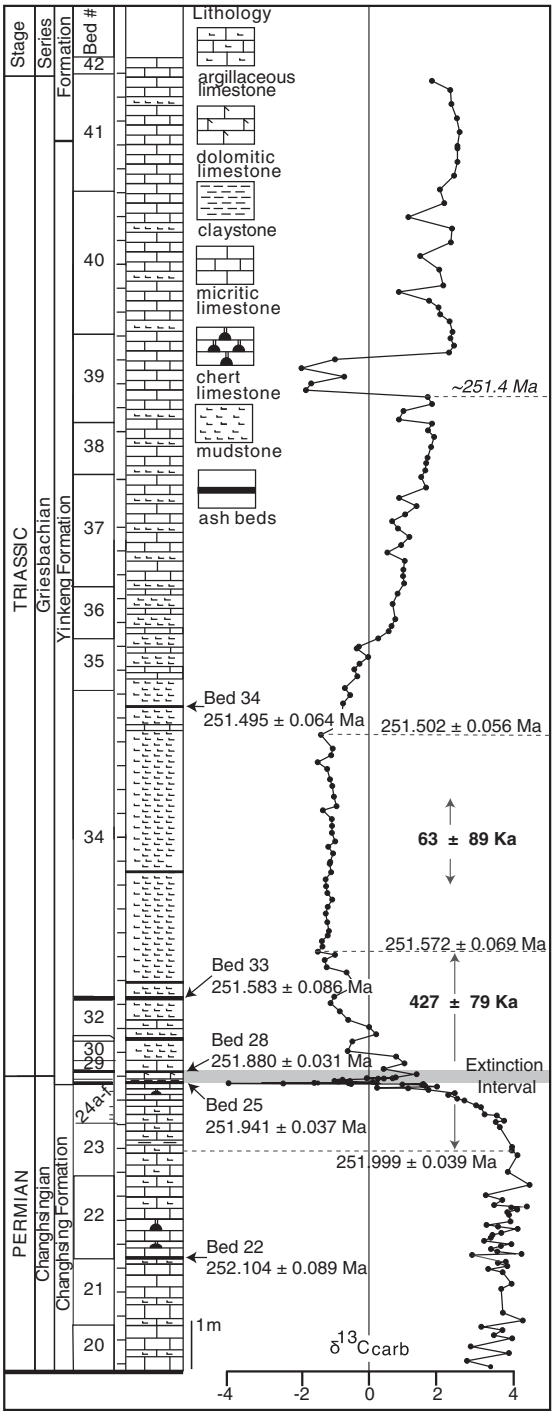

Fig. 1. Stratigraphy, geochronology, and carbonate carbon isotopic composition for the Permian-Triassic GSSP at Meishan, China. The Permian-Triassic GSSP from late Changshingian to Greisbachian showing weighted mean $^{206}Pb/^{238}U$ dates from this work adjacent to the stratigraphic column from Cao et al. (11). Datums between dated ash beds are calculated assuming constant sediment accumulation rates. Datum not bracketed by dated beds, such as the $\delta^{13}C_{carb}$ anomaly above Bed 34–2, is calculated using the sediment accumulation rate derived from the interval between the two stratigraphically closest ash beds. Uncertainty on interpolated dates is calculated using a Monte Carlo simulation, which exploits stratigraphic superposition of dated rocks (30). Uncertainty on durations/differences is added in quadrature from 2σ analytical uncertainty on dated beds.

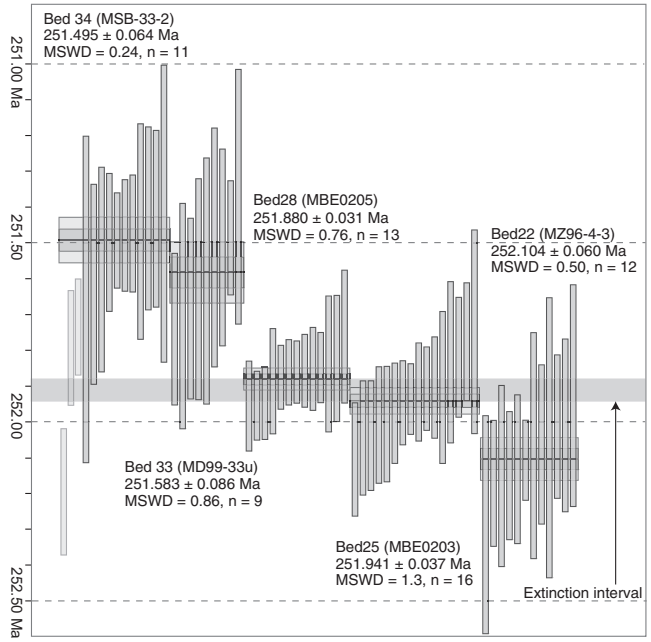

Fig. 2. Weighted mean calculated $^{206}Pb/^{238}U$ dates. Each vertical bar represents a single zircon analysis included in the weighted mean calculation for that sample. The height of each bar is proportional to the 2σ analytical uncertainty. The thin black line through each population of single grains is the weighted mean calculated date. Shaded horizontal bars above and below the weighted mean represent 1σ and 2σ analytical uncertainty. The shaded bar through all populations represents the maximum extinction interval. Light gray analysis is not included in the weighted mean calculation.

published in Shen et al. (3) (*SI Text*) and present more precise and accurate dates on zircon crystals isolated from five volcanic layers (beds 22, 25, 28, 33, and 34) that span the main extinction event, the major negative excursion and oscillation in $\delta^{13}C_{carb}$, the Permian-Triassic boundary at Meishan as defined by the first appearance datum (FAD) of the conodont, *Hindeodus parvus,* and the earliest Triassic period (Figs. 1 and 2 and Figs. S1 and S2).

New Age Model

We rely on weighted mean $^{206}Pb/^{238}U$ dates as the best estimate of eruption/depositional ages for these volcanic rocks. For each sample, we determined a minimum of nine dates on single grains of zircon, allowing recognition of outliers due to either incorporation of older zircon or open system behavior, such as Pb loss (Fig. 2, Table 1, and Tables S1 and S2). The individual $^{206}Pb/^{238}U$ dates and the calculated weighed mean $^{206}Pb/^{238}U$ dates we present for beds 22, 25, and 28 are distinctly younger (up to 0.2%) and more precise than dates on the same ash beds published in Shen et al. (3) (Table S1 and Fig. S2). We also present a weighted mean $^{206}Pb/^{238}U$ date on bed 33, which did not yield a reliable date in the previous study (3). The differences in age and precision reported here reflect adoption of major improvements in the way our U-Pb isotopic data are acquired and reduced, including use of the precisely calibrated EARTHTIME ^{202}Pb-^{205}Pb-^{233}U-^{235}U tracer solution, changes in the isotopic compositions of standards used to calibrate the tracer, new error propagation algorithms, and improved data acquisition and reduction techniques (23–25). Application of these improvements, discussed in detail in the *SI Text*, yields significantly improved accuracy and precision on the weighted mean and interpolated dates (Table S1 and Fig. S2). Uncertainties associated with weighted mean $^{206}Pb/^{238}U$ dates are reported as $\pm x/y/z$, where x is the analytical (internal) uncertainties and y and z include the systematic uncertainties associated with

Table 1. $^{206}Pb/^{238}U$ weighted mean dates for Meishan ash beds, sediment accumulation rates, and calculated datum

Stratigraphic locations and intervals	Ages of ash beds and datums, accumulation rates, and statistical parameters
Sample	Mya, *n*; MSWD
Bed 22-MZ96(-4.3)	252.104 ± 0.060/0.28 (12; 0.50)
Bed 25-MBE0203	251.941 ± 0.037/0.28 (16; 1.3)
Bed 28-MBE0205	251.880 ± 0.031/0.28 (13; 0.76)
Bed 33-MD99-3u	251.583 ± 0.086/0.29 (9; 0.86)
Bed 34-MSB34-2	251.495 ± 0.064/0.29 (11,0.24)
Sediment accumulation rates	Maximum-minimum (cm/ka)
Bed 22-25	2.6, 1.6–6.5
Bed 25-28	0.36, 0.17 - unconstrained
Bed 28-33	0.58, 0.34–0.95
Bed 33-34	6.8, 2.5 - unconstrained
Calculated datums and durations	
Abrupt decline in $\delta^{13}C_{carb}$ in bed 24e	251.950 ± 0.042 Mya
FAD *Hindeodus parvus* at GSSP, Meishan	251.902 ± 0.024 Mya
$\delta^{13}C_{carb}$ anomaly onset above Bed 34–2	~251.4 Mya
Extinction interval	0.061 ± 0.048 Mya
Carbonate carbon isotope excursion duration	2.1–18.8 ka

Datums between dated ash beds are calculated assuming constant sediment accumulation rates. Datums not bracketed by dated beds, such as the $\delta^{13}C_{carb}$ anomaly above bed 34-2, are calculated using the sediment accumulation rate derived from the interval between the two stratigraphically closest ash beds (Fig. 1). Dates calculated by assuming a constant sediment accumulation rate have unquantifiable uncertainties associated with depositional hiatuses. Thus, we apply a constant accumulation rate for datums between dated beds and indicate a maximum and minimum accumulation rate and age for datums not bracketed by dated beds. Uncertainty on interpolated dates and durations are calculated using a Monte Carlo simulation, which exploits stratigraphic superposition of dated rocks (30). Uncertainty on durations/differences is added in quadrature from 2σ analytical uncertainty on dated beds. MSWD, mean square of weighted deviates.

tracer calibration (0.03%) and ^{238}U decay constant (0.05%), respectively. If calculated dates are to be compared with other U-Pb laboratories not using the EARTHTIME tracer, then ±*y* should be used for each laboratory. If compared with other chronometers such as Ar-Ar or astrochronology, then ±*z* should be used.

The section at Meishan has long been recognized as being highly condensed, implying that calculated sediment accumulation rates may not accurately account for hiatuses between dated ash horizons (3). In agreement with Shen et al. (3), Jin et al. (26), and Wang et al. (27), we define the onset of extinction at the base of bed 25 and the end of the main extinction interval at bed 28. In other sections with higher accumulation rates such as Penglaitan (China) (3) and Gartnerkofel core (Swiss Alps) (28, 29), the extinction appears more abrupt; thus, our duration estimate between bed 25 and bed 28 at Meishan of 61 ± 48 ka is a maximum (Table 1, Fig. 1, and Fig. S1). This estimate is three times shorter than reported by Shen et al. (3) (Figs. S1 and S2) and is more consistent with the recent estimate derived from astrochronology of 83 ka (20).

The new geochronology permits a detailed examination of the relationships between the extinction, the isotopic composition of carbonate carbon, and its rate of change. The carbon isotope record is characterized by a negative shift in composition beginning just above the base of bed 23 (251.999 ± 0.039 Mya), 60 (−17/+56) ka before the beginning of the mass extinction interval, from +3–4‰ toward the lighter values (~ −1‰) that characterize the earliest Triassic (Fig. 1 and Fig. S1). $\delta^{13}C_{(carb)}$ drops off rapidly in the upper 6 cm of bed 24e, from +2 to ~ −4 ‰ (Fig. 1 and Fig. S1). In many sections that lack detailed paleontology and geochronology, this negative excursion is used to mark the onset of the extinction interval. The negative shift and subsequent rebound has a duration of between 2.1 and 18.8 ka depending on accumulation rate, slightly predating the beginning of the maximum extinction interval. Immediately following the initial large negative excursion, carbonate carbon isotopic composition oscillates (±1–2‰), until ~1 m above bed 33. Using an accumulation rate derived from interpolating between dated beds 33 and 34, this period of oscillation lasts until 251.572 ± 0.069 Mya, a duration of 427 ± 79 ka. [Uncertainty on interpolated dates is calculated using a Monte Carlo simulation, which exploits stratigraphic superposition of dated rocks (30).] For the remainder of bed 34, ~5 m of mudstone and micritic limestone, the $\delta^{13}C_{(carb)}$ is constant at ~ −1‰, in contrast to the +3–4‰ that characterizes the preextinction interval (Fig. 1). The $\delta^{13}C_{(carb)}$ composition then rises gradually starting at ~251.5, just below the dated ash within bed 34 and increases to the top of bed 39 where it is interrupted by a sharp, short-lived decrease calculated to have begun ~251.4 Mya (Fig. 1). Above this perturbation, $\delta^{13}C_{(carb)}$ remains at ~1‰ for the remainder of the Griesbachian. The negative excursion within bed 39 at Meishan was not recognized by Cao et al. (11) or Xie et al. (17) due to sample spacing, although more closely spaced sampling reported in Song et al. (31) recovers it. The second excursion is possibly correlative with one seen in the GK-1 core from the Carnic Alps (32), although this excursion cannot yet be confirmed as a global signal or to be useful in correlation. The total duration of volatility in the carbonate carbon record from the initial negative inflection within bed 23 to the relatively stable positive values in the top of bed 39 is a minimum of 500 ka. Significant changes in lithology above the dated bed suggest that the sediment accumulation rate calculated between beds 32 and 34 is likely not applicable for this interval. As such, the duration represented by this interval of rock is uncertain, and our estimated duration for the entire interval is a minimum (Fig. 1).

Sea surface paleotemperature increases ~10 °C (~23–33 °C) over the extinction interval (9, 33), beginning near the base of bed 25 and continuing into the early Triassic (Fig. S1). Sea

surface temperatures are estimated to have reached ~33 °C by bed 28, coinciding with the end of the mass extinction interval, and continued to rise until at least 251.583 ± 0.086 Mya (bed 33) (9). Calcium isotopic composition ($\delta^{44/40}Ca‰_{\text{bulk earth}}$) also varies over the extinction interval, and when coupled with apparent physiological selectivity of the extinction and an absence of reef builders in the early Triassic, these data have been interpreted to support rapid acidification of the surface ocean coincident with the mass extinction (4, 12).

Discussion

The efficacy of many proposed kill mechanisms, such as synchronous sea surface and atmospheric temperature increase, rapid rise in pCO_2, and flooding of shelf areas with anoxic and euxinic waters, depends on rate of change and on precisely when they occur relative to the onset of extinction (9, 34, 35). For example, it is crucial to know whether the ~10 °C increase in sea surface temperature close to the extinction interval slightly predates or postdates the onset of the mass extinction (9, 33) (Fig. S1). More detailed study of the relationship between temperature increase and extinction is needed from less condensed sections than Meishan to evaluate whether temperature leads or lags the extinction and the relationship between temperature rise and changes in the carbonate carbon isotopic record. Using the maximum extinction duration of ~60 ka, this suggests an ~1 °C increase per 6,000 y, comparable to the rate and magnitude of the increase at the Paleocene–Eocene Thermal Maximum (PETM) (36) and Pleistocene/Holocene postglacial warming (~2 °C/5 ka) (37). Tracking with temperature increase is a negative shift in $\delta^{44/40}Ca$, interpreted as resulting in part from acidification of the ocean over this same interval and fluctuations in $\delta^{13}C_{(carb)}$, consistent with continued volatility in the carbon cycle after the initial spike toward lighter composition in the top of bed 24e (4, 12) (Fig. 1 and Fig. S1). Thus, in 80 ± 45 ka (base of bed 24e → base of bed 28), there was a short-lived episode of major light carbon addition to the oceans, a major mass extinction, a rapid, dramatic increase in marine and terrestrial temperature, isotopic and biological evidence for ocean acidification, and a major shift in $\delta^{13}C_{(carb)}$ composition from an average of approximately + 3.5‰ in the late Permian to approximately −1‰ in the earliest Triassic, until 251.502 ± 0.056 Mya. The observation that the terrestrial and marine extinctions occurred simultaneously (3) and the suggestion that the sequence of extinction can be correlated with metabolic rate (1, 4) support the conclusion that rapidly elevated atmospheric pCO_2 and ocean/atmosphere temperatures drove a combination of kill mechanisms. However, whether the temperature increase leads, is synchronous with, or postdates the extinction is not yet known with sufficient precision. Although recovery and diversification in Ammonoids began in the earliest Triassic, the broad effects of this short-lived extinction or ecological restructuring persist for 5–10 My after the main extinction interval, emphasizing the evolutionary irreversibility of the event (38–41).

Many have proposed that the end-Permian extinction was triggered by the eruption/intrusion of the Siberian Traps Large Igneous Province, which is hypothesized to have been of short (~1–2 Ma) duration, to have occurred at approximately the same time as the extinction, and to have generated the large volume of volatiles via degassing of lavas and sediments required to drive such dramatic atmospheric and biotic response (2, 8, 42–46). The end-Permian extinction event occurred suddenly and rapidly (61 ± 48 ka) in an interval much shorter than current estimates for the total duration of Siberian Traps magmatism, suggesting that, similar to the end-Triassic extinction event, a single pulse of magmatism may be the most critical for triggering dramatic environmental change (43, 47, 48). Current U-Pb and Ar-Ar constraints on the timing and tempo of Siberian Traps magmatism are less precise by an order of magnitude than our new constraints on the extinction. With current estimates, it can only be concluded that magmatism either overlaps with or postdates the extinction (43, 47, 49). Additionally, the potential for bias between chronometers and subtle differences in calculated dates generated by single or multiple laboratories using different U-Pb data acquisition and reduction protocols currently prohibits exploring the full details of a causal relationship.

Payne and Kump (45) and Song et al. (50) hypothesized that the large volatility in the carbon cycle that dominates the interval from the beginning of the Dienarian through the Spathian is distinct from the extinction interval represented at the GSSP and likely represents new injection of light carbon and global warming–driven anoxia related to continued activity of the Siberian Traps Large Igneous Province, ~1 My after the extinction (Fig. 3). However, neither study had sufficient temporal control on the carbon isotope excursions or the age of Siberian volcanism to further evaluate this hypothesis. Here we demonstrate that upper bed 34 (mid-Griesbachian) is 251.495± 0.064, which predates the second negative excursion in $\delta^{13}C_{(carb)}$ at Meishan by ~100 ka if the sediment accumulation rate between beds 32 and 34 is applied. The large positive oscillation in $\delta^{13}C_{(carb)}$ (+6) observed by Payne et al. (51) and Meyer et al. (52) in southern China begins at about

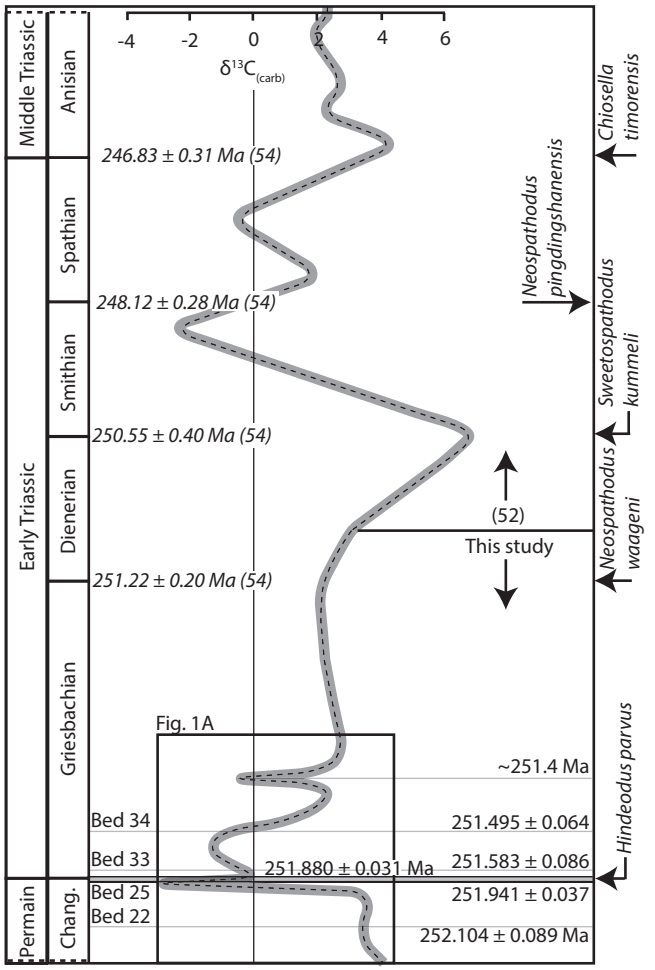

Fig. 3. Changshingian to Anisian carbonate carbon isotopic value from Meishan, China. Bed thickness, stratigraphic depth, lithology, and bed number from Cao et al. (11). Weighted mean $^{206}Pb/^{238}U$ dates are shown to the right of the stratigraphic column, and the maximum extinction duration is shaded in gray. Carbonate carbon isotopic composition in dotted gray line (11). Permian and Triassic conodont zones from Ogg (63). Stage/substage names are global standard chronostratigraphic units used by the International Commission on Stratigraphy.

the Griesbachian/Dienerian boundary and continues through the Dienerian before swinging to values of ~ −2‰ near the top of the Smithian (Fig. 3). Existing geochronology on the lower Smithian includes an age of 251.22 ± 0.2 (53, 54) (Fig. 3). If correct, this requires the entire Dienerian and part of the Greisbachian to have been deposited in ~300 ka. As shown here (see *SI Text*), use of the recalibrated EARTHTIME tracer and adoption of EARTHTIME protocols may in some cases result in dates that are 200–500 ka younger than those reported before adoption of these methods. Until dates from the Smithian are repeated using latest EARTHTIME protocols and tracer, it is probably unwise to combine/compare data. Nonetheless, we are confident that the large positive-negative oscillations that begin at the Griesbachian/Dienerian boundary are −251 Mya or younger, based on upward extrapolation from our dated ash beds at Meishan (Fig. 3). Thus, it is clear that these anomalies are ~1 Mya or more younger than the main extinction event and separated from the volatility characterizing this interval by a relatively stable plateau of $\delta^{13}C_{(carb)}$ at ~2‰ from the top of the second excursion in the Griesbachian to the Griesbachian/Dienerian boundary, whereupon the reservoir rises to values of 6‰ by the close of the Dinerian (Fig. 3). Meyer et al. (55) use coupled $\delta^{13}C_{org}$ and $\delta^{13}C_{carb}$ records from South China to support a causal connection between carbon isotope stabilization and enhanced biotic recovery in Middle Triassic time. Whether postextinction carbon cycle dynamics are being driven by intrinsic (biological) or extrinsic (environmental) forces before final restructuring in the early Anisian (~247 Mya) remains unclear. Integration of a calibrated carbon isotope record into the middle and late Triassic with an improved age model for the Siberian Traps will be required to evaluate this question.

When the end-Permian extinction is compared with other short-lived events such as the end-Triassic and end-Cretaceous extinctions and the PETM, we see in common, a short-lived perturbation of the carbon cycle followed by a rise in atmospheric pCO_2 and temperature, evidence for ocean acidification, anoxia, and rapid extinction (10s of thousands of years) (48, 56, 57). Recovery or restructuring (±additional extinction) occurs over an ~3-Mya timescale for the end-Triassic event and over as much as 5 Mya for the full recovery of marine fauna after the end Cretaceous, whereas full recovery from the end-Permian extinction may have taken as long as 5–10 My (39, 58, 59). A key question is whether the observed sequence is related to a common trigger such as volcanism or whether it less a function of mechanism and more fundamentally related to cascades of multiple feedbacks between intrinsic and extrinsic drivers. For all extinctions, understanding the timescales of extinction, the filling and restructuring of postextinction ecospace, and full recovery in different bathymetric and geographic settings is crucial and may be the key to understanding the truly singular and irreversible nature of the end-Permian event, as well as providing better context for the next millennium. We now have the geochronological tools to explore these feedbacks at the millennial to decamillenial timescales, which will in turn encourage higher-resolution chemostratigraphy to be obtained and allow detailed evaluation of more general models for mass extinction.

Conclusion

Our age model for the end-Permian extinction provides a precise and accurate timeline for the sequence of events at the end of the Permian, including carbon cycle reorganization, the main extinction event, a dramatic increase in global sea surface and atmospheric temperatures, possible ocean acidification, and a framework for exploring the cause and effects of the environmental changes and feedbacks that led to the greatest Phanerozoic mass extinction. The extinction had a duration of 61 ± 48 ka and was preceded by the onset of a rapid reorganization of the carbon cycle, including a rapid negative spike in $\delta^{13}C_{(carb)}$ of 3‰ lasting between 2.1 and 18.8 ka and a global shift in $\delta^{13}C_{(carb)}$ from approximately +4‰ το −1.5‰, with a duration of 427 ± 79 ka. This record represents a potentially characteristic $\delta^{13}C_{(carb)}$ topology for the end-Permian event, which will stimulate refined comparison with other Permian-Triassic sections, although the highly condensed nature of the Meishan section makes comparison with other sections difficult. The timing of the extinction and associated changes in environmental conditions are consistent with a very rapid biological response to environmental change followed by a complex recovery/restructuring period that took some 10 Ma for many species (38–41) and established the ecosystems that would dominate the Mesozoic. Further integration of the extinction timescale with detailed chemostratigraphic, cyclostratigraphic, and paleobiological data should allow many more insights into the dynamics and timing of extinction and restructuring. In addition, it is clear that more and higher precision geochronology from additional stratigraphic sections is needed. We predict that with further work will come the deconvolution of the end-Permian extinction into a cascade of smaller, shorter-lived extinction and recovery events, driven by differences in paleogeography, biology, and environmental degradation. The short-lived nature of the extinction, protracted nature of the recovery, and comparison with other extinction events suggests that environmental conditions preceding the largest of the Phanerozoic mass extinctions must have crossed a critical threshold or "tipping point" from which the biosphere was unable to recover or adapt quickly enough to survive.

Methods

Zircon crystals were separated from bulk samples using a combination of ultrasonic disaggregation and pulverization using a shatterbox, which was followed by magnetic separation, standard heavy-liquid separation, and careful selection of crystals under a microscope. Following thermal annealing at 900 °C for 60 h, each zircon crystal was placed into a 200-μL Teflon microcapsule and leached in 29 M hydrofluoric (HF) inside high-pressure Parr vessels held at 220 °C for 12 h, a procedure modified after the Chemical Abrasion partial-dissolution procedure of Mattinson (60). Grains were then transferred to 3-mL Savillex PFA beakers and rinsed with 16 M HNO_3 and 6 M HCl and fluxed in the acid at 80 °C, followed by a 30-min ultrasonic bath. Between acid washes, grains were rinsed with Milli-Q water. Single zircon crystals were loaded with clean water into teflon microcapsules and spiked with the EARTHTIME ^{202}Pb-^{205}Pb-^{233}U-^{235}U (ET2535) tracer solution and dissolved in 29 M HF at 220 °C for 48 h. On dissolution, aliquots were dried down on a hotplate and redissolved under pressure in 6 M HCl overnight at 180 °C. Sample solutions were then dried and redissolved at 80 °C in 3 N HCl. Lead and U were separated using a miniaturized HCl-based ion-exchange chromatography procedure modified from Krogh (61) with 40-μL columns of AG1 × 8 resin. Eluted U and Pb were dried down with H_3PO_4 and then redissolved in a silica gel emitter solution (62) and loaded onto a zone-refined, outgassed Re filament. Measurement of isotopic ratios was done on an IsotopX ×62 multiple-collector thermal ionization mass spectrometer. Isotopes of Pb were measured by peak-hopping on a single Daly/photomultiplier detector system. Isotopes of U were measured as UO_2 on Faraday detectors in static mode. Isotope ratios of U and Pb were corrected for mass fractionation during analysis using the ET2535 tracer solution. Data acquisition and reduction were done using the Tripoli and U-Pb Redux software packages (24, 25).

ACKNOWLEDGMENTS. We thank Dan Rothman for discussions and two anonymous reviewers for comments. This work was supported by National Science Foundation Continental Dynamics Grant EAR-0807475 (to S.B.) and Instrumentation and Facilities EAR-0931839 (to S.B.). Additional support was provided from National Aeronautics and Space Administration Astrobiology Grant NNA08CN84A (to S.B.) and National Natural Science Foundation of China Grant 41290260 (to S.-z.S.). This work benefitted from the efforts of the EARTHTIME U-Pb community.

1. Knoll AH, Bambach RK, Payne JL, Pruss S, Fischer WW (2007) Paleophysiology and end-Permian mass extinction. *Earth Planet Sci Lett* 256(3-4):295–313.

2. Wignall PB (2007) The end-Permian mass extinction: How bad did it get? *Geobiology* 5(4):303–309.

3. Shen SZ, et al. (2011) Calibrating the end-Permian mass extinction. *Science* 334(6061): 1367–1372.
4. Payne JL, Clapham ME (2012) End-Permian mass extinction in the oceans: An ancient analog for the twenty-first century? *Annu Rev Earth Planet Sci* 40:89–111.
5. Erwin DH (1998) The end and the beginning: Recoveries from mass extinctions. *Trends Ecol Evol* 13(9):344–349.
6. Erwin DH (2006) *Extinction: How Life on Earth Nearly Ended 250 Million Years Ago* (Princeton Univ Press, Princeton).
7. Knoll AH, Fischer WW (2011) Skeletons and ocean chemistry: The long view. *Ocean Acidification*, eds Gattuso JP, Hansson L (Oxford University Press, New York), pp 67–82.
8. Brand U, et al. (2012) The end-Permian mass extinction: A rapid volcanic CO2 and CH4-climatic catastrophe. *Chem Geol* 322-323:121–144.
9. Joachimski MM, et al. (2012) Climate warming in the latest Permian and the Permian-Triassic mass extinction. *Geology* 40:195–198.
10. Georgiev S, et al. (2011) Hot acidic Late Permian seas stifle life in record time. *Earth Planet Sci Lett* 310(3-4):389–400.
11. Cao C, et al. (2009) Biogeochemical evidence for euxinic oceans and ecological disturbance presaging the end-Permian mass extinction event. *Earth Planet Sci Lett* 281(3-4):188–201.
12. Hinojosa JL, et al. (2012) Evidence for end-Permian ocean acidification from calcium isotopes in biogenic apatite. *Spec Pap Geol Soc Am* 40(8):743–746.
13. Bowring SA, Erwin DH, Davidek K, Wang W, Jin MW, Martin YG (1998) U/Pb zircon geochronology and tempo of the end-permian mass extinction. *Science* 280(5366): 1039–1045.
14. Mundil R, et al. (2001) Timing of the Permian–Triassic biotic crisis: Implications from new zircon U/Pb age data (and their limitations). *Earth Planet Sci Lett* 187(1-2):131–145.
15. Mundil R, Ludwig KR, Metcalfe I, Renne PR (2004) Age and timing of the Permian mass extinctions: U/Pb dating of closed-system zircons. *Science* 305(5691):1760–1763.
16. Twitchett RJ, Looy CV, Morante R, Visscher H, Wignall PB (2001) Rapid and synchronous collapse of marine and terrestrial ecosystems during the end-Permian biotic crisis. *Geology* 29(4):351–354.
17. Xie S, et al. (2007) Changes in the global carbon cycle occurred as two episodes during the Permian–Triassic crisis. *Spec Pap Geol Soc Am* 35(12):1083–1086.
18. Huang C, Tong J, Hinnov L, Chen ZQ (2011) Did the great dying of life take 700 k.y.? Evidence from global astronomical correlation of the Permian-Triassic boundary interval. *Geology* 39(8):779–782.
19. Rampino MR, Kaiho K (2012) Did the great dying of life take 700 k.y.? Evidence from global astronomical correlation of the Permian-Triassic boundary interval. *Geology Forum* 40(5):e267.
20. Wu H, et al. (2013) Time-calibrated Milankovitch cycles for the late Permian. *Nat Commun* 4:2452.
21. Wang Y, et al. (2013) Quantifying the process and abruptness of the end-Permian mass extinction. *Paleobiology* 40(1):113–129.
22. Jin YG, et al. (2006) The global boundary stratotype section and point (GSSP) for the base of Changhsingian stage (upper Permian). *Episodes* 29(4):175–182.
23. Condon DJ, McLean N, Noble SR, Bowring SA (2010) Isotopic composition (238U/235U) of some commonly used uranium reference materials. *Geochim Cosmochim Acta* 74(24):7127–7143.
24. McLean N, Bowring J, Bowring S (2011) An algorithm for U-Pb isotope dilution data reduction and uncertainty propagation. *Geochem Geophys Geosyst* 12(6):1–26.
25. Bowring JF, McLean NM, Bowring SA (2011) Engineering cyber infrastructure for U-Pb geochronology: Tripoli and U-Pb_Redux. *Geochem Geophys Geosyst* 12(6):1–19.
26. Jin YG, et al. (2000) Pattern of marine mass extinction near the Permian-Triassic boundary in South China. *Science* 289(5478):432–436.
27. Wang Y, et al. (2013) Quantifying the process and abruptness of the end-Permian mass extinction. *Paleobiology* 40(1):113–129.
28. Rampino MR, Prokoph A, Adler A (2000) Tempo of the end-Permian event: High-resolution cyclostratigraphy at the Permian-Triassic boundary. *Geology* 28(7):643–646.
29. Gorjan P, Kaiho K, Chen ZQ (2007) A carbon-isotopic study of an end-Permian mass-extinction horizon, Bulla, northern Italy: A negative δ 13C shift prior to the marine extinction. *Terra Nova* 244(3-4):483–492.
30. Guex J, et al. (2008) Geochronological constraints on post-extinction recovery of the ammonoids and carbon cycle perturbations during the Early Jurassic. *Palaeogeogr Palaeoclimatol Palaeoecol* 267(1-2):266–275.
31. Song H, et al. (2013) Large vertical δ13CDIC gradients in Early Triassic seas of the South China craton: Implications for oceanographic changes related to Siberian Traps volcanism. *Global Planet Change* 105:7–20.
32. Korte C, et al. (2004) Carbon, sulfur, oxygen and strontium isotope records, organic geochemistry and biostratigraphy across the Permian/Triassic boundary in Abadeh, Iran. *Int J Earth Sci* 93(4):565–581.
33. Sun Y, et al. (2012) Lethally hot temperatures during the Early Triassic greenhouse. *Science* 338(6105):366–370.
34. Kiehl JT, Shields CA (2005) Climate simulation of the latest Permian: Implications for mass extinction. *Geology* 33(9):757.
35. Wignall PB, Twitchett RJ (1996) Oceanic anoxia and the end Permian mass extinction. *Science* 272(5265):1155–1158.
36. Zeebe RE, Zachos JC, Dickens GR (2009) Carbon dioxide forcing alone insufficient to explain Palaeocene–Eocene thermal maximum warming. *Nat Geosci* 2:576–580.
37. Lea DW, Pak DK, Spero HJ (2000) Climate impact of late quaternary equatorial pacific sea surface temperature variations. *Science* 289(5485):1719–1724.
38. Payne JL, et al. (2011) Early and middle triassic trends in diversity, evenness, and size of foraminifers on a carbonate platform in south china: Implications for tempo and mode of biotic recovery from the end-permian mass extinction. *Paleobiology* 37(3): 409–425.
39. Chen ZQ, Benton MJ (2012) The timing and pattern of biotic recovery following the end-Permian mass extinction. *Nat Geosci* 5:375–383.
40. Song H, et al. (2011) Recovery tempo and pattern of marine ecosystems after the end-Permian mass extinction. *Geology* 39(8):739–742.
41. Brayard A, et al. (2009) Good genes and good luck: Ammonoid diversity and the end-Permian mass extinction. *Science* 325(5944):1118–1121.
42. Svensen H, et al. (2009) Siberian gas venting and the end-Permian environmental crisis. *Earth Planet Sci Lett* 277(3-4):490–500.
43. Kamo SL, et al. (2003) Rapid eruption of Siberian flood-volcanic rocks and evidence for coincidence with the Permian–Triassic boundary and mass extinction at 251 Ma. *Earth Planet Sci Lett* 214:75–91.
44. Ganino C, Arndt NT (2009) Climate changes caused by degassing of sediments during the emplacement of large igneous provinces. *Chem Geol* 37:323–326.
45. Payne J, Kump L (2007) Evidence for recurrent Early Triassic massive volcanism from quantitative interpretation of carbon isotope fluctuations. *Earth Planet Sci Lett* 256(1-2):264–277.
46. Renne PR, Black MT, Zichao Z, Richards MA, Basu AR (1995) Synchrony and causal relations between permian-triassic boundary crises and siberian flood volcanism. *Science* 269(5229):1413–1416.
47. Reichow MK, et al. (2009) The timing and extent of the eruption of the Siberian Traps large igneous province: Implications for the end-Permian environmental crisis. *Earth Planet Sci Lett* 277(1-2):9–20.
48. Blackburn TJ, et al. (2013) Zircon U-Pb geochronology links the end-Triassic extinction with the Central Atlantic Magmatic Province. *Science* 340(6135):941–945.
49. Ivanov AV, et al. (2013) Siberian Traps large igneous province: Evidence for two flood basalt pulses around the Permo-Triassic boundary and in the Middle Triassic, and contemporaneous granitic magmatism. *Earth Sci Rev* 122:58–76.
50. Song H, Wignall PB, Tong J, Yin H (2013) Two pulses of extinction during the Permian–Triassic crisis. *Nat Geosci* 6:52–56.
51. Payne JL, et al. (2004) Large perturbations of the carbon cycle during recovery from the end-permian extinction. *Science* 305(5683):506–509.
52. Meyer KM, Yu M, Jost AB, Kelley BM, Payne JL (2011) δ13C evidence that high primary productivity delayed recovery from end-Permian mass extinction. *Earth Planet Sci Lett* 302(3-4):378–384.
53. Galfetti T, et al. (2007) Smithian-Spathian boundary event: Evidence for global climatic change in the wake of the end-Permian biotic crisis. *Geology* 35(4):291–294.
54. Ovtcharova M, et al. (2006) New Early to Middle Triassic U–Pb ages from South China: Calibration with ammonoid biochronozones and implications for the timing of the Triassic biotic recovery. *Earth Planet Sci Lett* 243(3-4):463–475.
55. Meyer KM, Yu M, Lehrmann D, Van de Schootbrugge B, Payne JL (2013) Constraints on Early Triassic carbon cycle dynamics from paired organic and inorganic carbon isotope records. *Earth Planet Sci Lett* 361:429–435.
56. Zachos JC, Dickens GR, Zeebe RE (2008) An early Cenozoic perspective on greenhouse warming and carbon-cycle dynamics. *Nature* 451(7176):279–283.
57. Schulte P, et al. (2010) The Chicxulub asteroid impact and mass extinction at the Cretaceous-Paleogene boundary. *Science* 327(5970):1214–1218.
58. D'Hondt S (2005) Consequences of the Cretaceous/Paleogene mass extinction for marine ecosystems. *Annu Rev Ecol Evol Syst* 36:295–317.
59. Ruhl M, Deenen M, Abels HA, Bonis NR (2010) Astronomical constraints on the duration of the early Jurassic Hettangian stage and recovery rates following the end-Triassic mass extinction (St Audrie's Bay/East Quantoxhead, UK). *Earth Planet Sci Lett* 295(1-2):262–276.
60. Mattinson JM (2005) Zircon U–Pb chemical abrasion ("CA-TIMS") method: Combined annealing and multi-step partial dissolution analysis for improved precision and accuracy of zircon ages. *Chem Geol* 220(1-2):47–66.
61. Krogh TE (1973) A low-contamination method for hydrothermal decomposition of zircon and extraction of U and Pb for isotopic age determinations. *Geochim Cosmochim Acta* 37(3):485–494.
62. Gerstenberger H, Haase G (1997) A highly effective emitter substance for mass spectrometric Pb isotope ratio determinations. *Chem Geol* 136(3-4):309–312.
63. Ogg JG (2012) The Triassic period. *The Geologic Time Scale*, eds Gradstein FM, Ogg JG, Schmitz MD, Ogg G (Elsevier, New York), pp 681–730.

Supporting Information

Burgess et al. 10.1073/pnas.1317692111

SI Text

The calculated weighed mean $^{206}Pb/^{238}U$ dates from this study are younger than dates on the same ash beds published in ref. 1 by up to 0.2% (Table S1 and Fig. S2). This difference is 7–9 times the uncertainty associated with each weighted mean date. Here we explore possible explanations. To eliminate any potential issues with sample heterogeneity, we used the same mineral separates that were analyzed for ref. 1 and chose morphologically similar, high aspect ratio zircons. Both studies yield a similar distribution of single grain dates with an approximately normal distribution of errors [mean square of weighted deviates (MSWD) ≅ 1] when the few outliers interpreted to be the result of inheritance (n = 10/61) are excluded, and it is assumed that chemical abrasion effectively eliminates Pb loss in most cases. We consider it unlikely that the younger weighted mean dates seen in this work are the result of a selection bias or systematic Pb loss in multiple populations of zircon.

The data for ref. 1 were acquired in 2006, in the early stages of the EARTHTIME initiative. Since that time, there have been significant changes in the way U-Pb data are acquired and reduced at Massachusetts Institute of Technology and in other laboratories. These changes include the following. (*i*) New values for the isotopic compositions and purity of U and Pb standards used to calibrate the EARTHTIME tracer solution and new algorithms to determine this composition, which improves the accuracy of the solution calibration relative to the MIT1L calibration by ref. 2 and used in ref. 1. The new calibration reflects the ∼5 permil change in the $^{238}U/^{235}U$ values for CRM112a determined by ref. 3, which leads overall to a decrease in a single $^{206}Pb/^{238}U$ date of ∼0.05%. (*ii*) As a result of tracer calibration, we refined the $^{18}O/^{16}O$ ratio used for UO_2 measurements, which results in a value ∼2.5% greater than that used to reduce the data in ref. 1 and a 0.025% decrease (∼60 ka) in a typical single-grain $^{206}Pb/^{238}U$ date. (*iii*) Refined estimates of the isotopic composition and dispersion in the laboratory blank, which includes additional measurements and a revised algorithm to calculate composition, indicate that the composition used in ref. 1 was not as accurate as the values used in this study and that the uncertainties were underestimated. For example, applying the composition and uncertainty used by ref. 1 to data from bed 25 generated for this study results in an increase of the weighted mean $^{206}Pb/^{238}Pb$ date by 35 ka, with a 27% decrease in analytical uncertainty. (*iv*) New algorithms were used for point by point interference correction on masses 201–205. (*v*) Point by point fractionation corrections for Pb were used using the EARTHTIME 202-205-233-238 tracer rather than application of a single value for α-Pb based on long-term monitoring of National Bureau of Standards 981, 982, and synthetic zircon solutions with ET535 added, which was done in ref. 1. We suggest that the fractionation correction used in this study likely reduces scatter in $^{206}Pb/^{238}U$ dates caused by assuming a constant value and uncertainty. (*vi*) New algorithms were used for determining and propagating uncertainties into a weighted mean date (4, 5). The dates in ref. 1 cannot simply be recalculated to independently incorporate one or all of the above changes, and thus the relative effects of each cannot be evaluated.

The nonlinear difference between dates also suggests that the subjectivity of data reduction and other factors such as the response of zircon to chemical abrasion and/or subtle, unaccounted for interference corrections, may play a role. Application of these improvements yield significantly improved accuracy and precision on the weighted mean and interpolated dates (Fig. S2 and Table S2). This improvement is particularly evident for bed 33, on which no mean was calculated by ref. 1 due to excess scatter, which is likely due to residual Pb-loss (Fig. S2).

1. Shen SZ, et al. (2011) Calibrating the end-Permian mass extinction. *Science* 334(6061): 1367–1372.
2. Schoene B, Crowley JL, Condon DJ, Schmitz MD, Bowring SA (2006) Reassessing the uranium decay constants for geochronology using ID-TIMS U–Pb data. *Geochim Cosmochim Acta* 70(2):426–445.
3. Condon DJ, McLean N, Noble SR, Bowring SA (2010) Isotopic composition (238U/235U) of some commonly used uranium reference materials. *Geochim Cosmochim Acta* 74 (24):7127–7143.
4. McLean N, Bowring J, Bowring S (2011) An algorithm for U-Pb isotope dilution data reduction and uncertainty propagation. *Geochem Geophys Geosyst* 12(6):1–26.
5. Bowring JF, McLean NM, Bowring SA (2011) Engineering cyber infrastructure for U-Pb geochronology: Tripoli and U-Pb_Redux. *Geochem Geophys Geosyst* 12(6): 1–19.

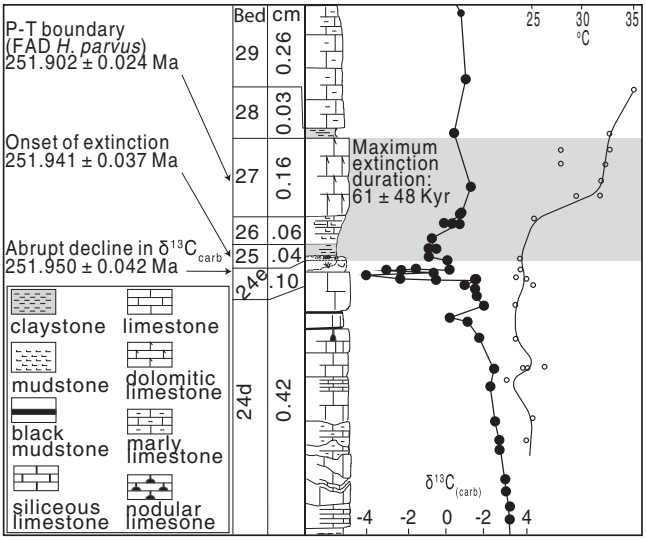

Fig. S1. Stratigraphy, geochronology, carbonate carbon isotopic composition, and composite ocean paleotemperature for the extinction interval at the Global Stratotype Section and Point (GSSP), Meishan, China. Stratigraphy and carbonate carbon isotopic composition are from Cao et al. (1). Paleotemperature is from Joachimski et al. (2).

1. Cao C, et al. (2009) Biogeochemical evidence for euxinic oceans and ecological disturbance presaging the end-Permian mass extinction event. *Earth Planet Sci Lett* 281(3-4):188–201.
2. Joachimski MM, et al. (2012) Climate warming in the latest Permian and the Permian-Triassic mass extinction. *Geology* 40(3):195–198.

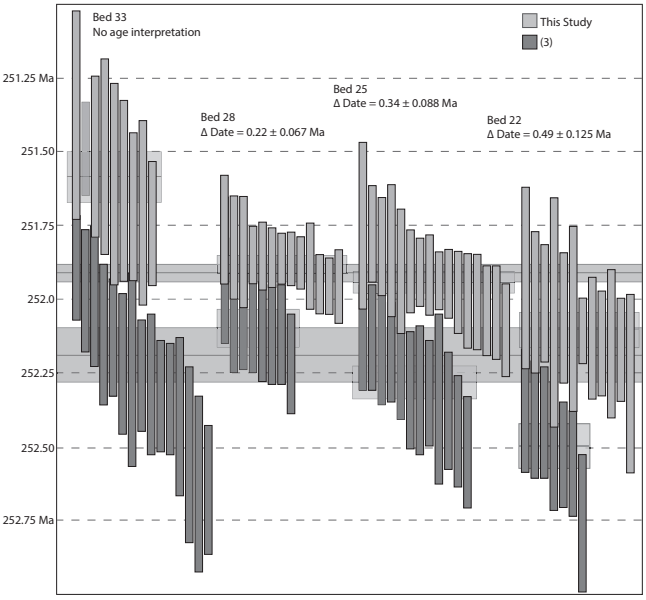

Fig. S2. Comparison of single-grain zircon analysis from beds 22, 25, 28, and 33. Dates from ref. 1 are in dark gray and from this study are in light gray. Each vertical bar represents a single zircon analysis, the height of which is proportional to the 2σ analytical uncertainty on that analysis. The thin horizontal bar through the middle of each population of analysis represents the weighted mean calculated date for that bed, which is surrounded by the 2σ analytical uncertainty on this date. Thick horizontal lines passing through the diagram are the calculated maximum extinction duration (beds 25–28) and are keyed by color to the respective study.

1. Shen SZ, et al. (2011) Calibrating the end-Permian mass extinction. *Science* 334(6061):1367–1372.

Table S1. Difference in $^{206}Pb/^{238}U$ weighted mean dates for Meishan ash beds from this study and from ref. 1

Sample	Shen et al. 2011	*n*; MSWD	Mya*	*n*; MSWD	ΔDate (Mya)
Bed 22-MZ96 (−4.3)	252.50 ± 0.11	(8; 0.8)	252.104 ± 0.060/0.28	(12, 0.50)	0.49 ± 0.125
Bed 25-MBE0203	252.28 ± 0.08	(13; 1.9)	251.941 ± 0.037/0.28	(16; 1.3)	0.34 ± 0.088
Bed 28-MBE0205	252.10 ± 0.06	(7; 1.4)	251.880 ± 0.031/0.28	(13; 0.76)	0.22 ± 0.067
Bed 33-MD99-33u	No age interpretation	Not applicable	251.583 ± 0.086/0.29	(9, 0.86)	None

*Uncertainty reported is 2σ internal (analytical)/external. External uncertainty includes uncertainty associated with tracer calibration and ^{238}U decay constant. Uncertainty on differences is added in quadrature from 2σ analytical uncertainty on dated beds.

1. Condon DJ, McLean N, Noble SR, Bowring SA (2010) Isotopic composition (238U/235U) of some commonly used uranium reference materials. *Geochim Cosmochim Acta* 74:7127–7143.

Table S2. U-Pb isotopic data and single-grain zircon dates

Sample and fraction	Composition			Isotopic ratios									Dates (Mya)				
	Pb* (pg)†	Pbc (pg)‡	Th/U§	206Pb/ 204Pb¶	208Pb/ 206Pb‖	206Pb/ 238U‖	±2s %	207Pb/ 235U‖	±2s %	207Pb/ 206Pb‖	±2s %	Correlation coefficient	206Pb/238U <Th>**f	±2s absolute††	207Pb/ 235U‡‡	±2s absolute††	Correlation coefficient
MD99-33u (bed 33)																	
z1	10.277	0.813	0.742	730.807	0.235	0.040	0.111	0.284	1.260	0.052	1.238	0.240	251.513	0.275	253.561	2.828	0.240
z2	9.475	0.839	0.592	679.826	0.187	0.040	0.125	0.283	1.351	0.052	1.329	0.221	251.630	0.309	252.952	3.025	0.221
z4	9.275	0.663	0.827	790.601	0.262	0.040	0.102	0.281	1.164	0.051	1.145	0.226	251.684	0.252	251.842	2.595	0.226
z5	5.586	0.552	0.644	603.426	0.204	0.040	0.135	0.280	1.531	0.051	1.505	0.238	251.513	0.334	251.029	3.406	0.238
z6	5.995	0.617	0.730	568.289	0.231	0.040	0.139	0.281	1.631	0.051	1.606	0.221	251.607	0.344	251.619	3.636	0.221
z9	12.836	0.523	0.717	1411.322	0.227	0.040	0.065	0.282	0.644	0.051	0.631	0.244	251.486	0.159	252.017	1.437	0.244
z11	8.236	0.745	0.655	655.293	0.207	0.040	0.128	0.284	1.392	0.052	1.370	0.221	251.705	0.315	253.751	3.126	0.221
z16	8.950	0.567	0.683	922.383	0.216	0.040	0.086	0.283	0.984	0.052	0.967	0.231	251.741	0.212	253.161	2.204	0.231
z17	7.186	0.762	0.733	551.292	0.232	0.040	0.144	0.279	1.689	0.051	1.658	0.253	251.371	0.356	249.986	3.743	0.253
MBE0205 (bed 28)																	
z1	95.822	0.313	0.478	18513.842	0.151	0.040	0.051	0.282	0.085	0.051	0.059	0.709	251.956	0.126	251.993	0.190	0.709
z4	12.658	0.442	0.723	1641.269	0.228	0.040	0.059	0.282	0.558	0.051	0.548	0.220	251.886	0.147	252.277	1.247	0.220
z6	18.890	0.958	0.592	1172.719	0.187	0.040	0.071	0.282	0.776	0.051	0.763	0.226	251.823	0.176	251.903	1.730	0.226
z8	37.429	0.562	0.607	3904.118	0.192	0.040	0.037	0.282	0.237	0.051	0.232	0.216	251.862	0.091	251.996	0.530	0.216
z11	27.572	0.530	0.684	2997.531	0.216	0.040	0.036	0.281	0.305	0.051	0.299	0.208	251.875	0.089	251.842	0.680	0.208
z12	11.461	0.574	0.731	1147.501	0.231	0.040	0.075	0.281	0.796	0.051	0.781	0.248	251.762	0.186	251.586	1.774	0.248
z13	17.787	0.983	0.465	1114.532	0.147	0.040	0.077	0.281	0.821	0.051	0.808	0.213	251.838	0.190	251.845	1.830	0.213
z16	23.831	0.578	0.548	2460.545	0.173	0.040	0.041	0.282	0.368	0.051	0.361	0.204	251.948	0.101	252.389	0.822	0.204
z17	26.153	0.529	0.500	2987.040	0.158	0.040	0.039	0.282	0.302	0.051	0.299	0.149	251.955	0.096	252.295	0.676	0.149
z18	19.001	0.388	0.660	2840.031	0.209	0.040	0.040	0.282	0.322	0.051	0.316	0.216	251.848	0.098	252.266	0.720	0.216
z21	23.401	0.415	0.524	3382.454	0.166	0.040	0.035	0.282	0.269	0.051	0.263	0.218	251.861	0.087	252.137	0.600	0.218
z23	41.944	1.133	0.629	2165.926	0.199	0.040	0.047	0.282	0.419	0.051	0.411	0.225	251.852	0.116	252.206	0.936	0.225
z25	22.163	0.528	0.526	2521.836	0.166	0.040	0.041	0.282	0.363	0.051	0.355	0.256	251.857	0.102	251.936	0.810	0.256
MBE0203 (bed 25)																	
z5	11.974	0.520	0.626	1355.706	0.198	0.040	0.062	0.283	0.670	0.052	0.658	0.226	252.038	0.153	253.146	1.500	0.226
z6	16.591	0.579	0.680	1659.969	0.215	0.040	0.057	0.282	0.546	0.051	0.537	0.215	251.976	0.140	252.106	1.220	0.215
z7	35.158	0.894	0.594	2321.304	0.188	0.040	0.047	0.282	0.390	0.051	0.381	0.236	251.947	0.117	252.501	0.872	0.236
z8	24.082	0.584	0.647	2398.111	0.205	0.040	0.055	0.282	0.384	0.051	0.374	0.244	251.917	0.137	252.477	0.859	0.244
z11	24.813	0.413	0.634	3503.291	0.201	0.040	0.040	0.282	0.263	0.051	0.256	0.232	251.936	0.099	252.195	0.588	0.232
z12	22.225	1.046	0.663	1240.030	0.210	0.040	0.066	0.283	0.727	0.051	0.716	0.220	252.009	0.163	252.744	1.627	0.220
z14	12.232	0.424	0.608	1700.375	0.192	0.040	0.115	0.281	0.563	0.051	0.535	0.336	251.748	0.284	251.503	1.254	0.336
z16	30.500	0.469	0.596	3822.666	0.189	0.040	0.047	0.281	0.256	0.051	0.246	0.295	251.907	0.116	251.733	0.571	0.295

Table S2. Cont.

Sample and fraction	Composition			Isotopic ratios									Dates (Mya)				
	Pb* (pg)†	Pbc (pg)‡	Th/U§	206Pb/ 204Pb¶	208Pb/ 206Pb‖	206Pb/ 238U‖	±2s %	207Pb/ 235U‖	±2s %	207Pb/ 206Pb‖	±2s %	Correlation coefficient	206Pb/238U <Th>**f	±2s absolute††	207Pb/ 235U‡‡	±2s absolute††	Correlation coefficient
z21	11.767	0.397	0.564	1766.638	0.178	0.040	0.067	0.282	0.517	0.051	0.508	0.208	251.776	0.165	251.913	1.154	0.208
z22	10.698	0.251	0.718	2433.824	0.227	0.040	0.065	0.283	0.409	0.052	0.399	0.222	252.005	0.161	253.275	0.916	0.222
z23	20.597	0.303	0.831	3763.472	0.263	0.040	0.064	0.282	0.277	0.051	0.267	0.265	252.045	0.160	252.109	0.619	0.265
z24	29.528	0.279	0.502	6363.726	0.159	0.040	0.091	0.282	0.193	0.051	0.164	0.527	251.833	0.225	252.184	0.432	0.527
z25	28.759	0.907	0.604	1870.738	0.191	0.040	0.064	0.282	0.490	0.051	0.479	0.234	252.105	0.158	252.142	1.095	0.234
z26	10.264	0.475	0.619	1276.525	0.196	0.040	0.086	0.282	0.754	0.051	0.736	0.257	251.904	0.212	252.468	1.685	0.257
z31	19.637	0.304	0.651	3742.086	0.206	0.040	0.053	0.284	0.276	0.052	0.265	0.283	252.766	0.131	253.648	0.619	0.283
z32	12.619	0.357	0.687	2041.178	0.217	0.040	0.079	0.282	0.473	0.051	0.464	0.190	252.717	0.195	252.501	1.056	0.190
z33	17.971	0.410	0.656	2543.477	0.207	0.040	0.057	0.282	0.375	0.051	0.368	0.185	251.904	0.141	252.193	0.837	0.185
z34	10.251	0.310	0.535	1986.473	0.169	0.040	0.068	0.282	0.484	0.051	0.477	0.182	251.820	0.167	252.533	1.083	0.182
z35	6.590	0.321	0.649	1203.960	0.205	0.040	0.095	0.283	0.821	0.051	0.803	0.246	252.534	0.234	252.923	1.839	0.246
MZ96 (–4.3) (bed 22)																	
z1	9.070	0.558	0.507	991.047	0.160	0.040	0.084	0.287	0.920	0.052	0.903	0.236	254.321	0.208	256.400	2.084	0.236
z2	19.219	0.495	0.423	2397.833	0.134	0.040	0.045	0.283	0.377	0.051	0.372	0.165	252.107	0.112	252.959	0.844	0.165
z3	8.175	0.597	0.504	839.435	0.159	0.040	0.102	0.283	1.088	0.052	1.069	0.229	252.151	0.253	253.409	2.440	0.229
z5	9.489	0.504	0.502	1146.177	0.158	0.052	0.074	0.385	0.767	0.054	0.757	0.175	326.432	0.237	330.723	2.164	0.175
z6	7.170	0.595	0.570	727.912	0.180	0.040	0.098	0.282	1.253	0.051	1.245	0.119	252.010	0.241	252.274	2.799	0.119
z7	5.595	0.463	0.416	759.359	0.131	0.040	0.125	0.282	1.214	0.051	1.192	0.231	251.927	0.310	252.314	2.713	0.231
z8	5.379	0.481	0.751	648.381	0.237	0.040	0.158	0.281	1.462	0.051	1.420	0.313	252.044	0.391	251.080	3.252	0.313
z9	1.922	0.651	0.448	2042.101	0.137	0.148	0.198	1.455	0.386	0.071	0.325	0.538	889.717	1.648	912.127	2.322	0.538
z10	9.062	0.655	0.458	857.181	0.145	0.040	0.090	0.283	1.063	0.052	1.045	0.236	252.063	0.222	253.086	2.381	0.236
z14	10.793	0.589	0.549	1103.944	0.174	0.040	0.081	0.278	0.860	0.051	0.838	0.307	252.013	0.200	249.129	1.899	0.307
z16	10.097	0.264	0.630	2241.185	0.199	0.040	0.072	0.282	0.456	0.051	0.438	0.318	252.150	0.179	252.035	1.017	0.318
z17	7.648	0.286	0.191	1763.883	0.061	0.040	0.084	0.282	0.615	0.051	0.589	0.369	252.132	0.208	252.225	1.373	0.369
z18	9.148	0.257	0.497	2154.042	0.157	0.040	0.071	0.282	0.446	0.051	0.443	0.128	252.172	0.176	252.478	0.998	0.128
z21	17.438	0.306	0.543	3390.630	0.171	0.059	0.091	0.446	0.377	0.055	0.357	0.323	370.678	0.329	374.652	1.180	0.323
z22	4.697	0.329	0.516	870.075	0.163	0.040	0.128	0.281	1.110	0.051	1.086	0.238	252.066	0.316	251.214	2.469	0.238
z23	5.777	0.446	0.677	759.931	0.214	0.040	0.123	0.284	1.207	0.052	1.191	0.180	252.287	0.305	253.836	2.711	0.180
MSB 34–2 (bed 34)																	
z9	27.946	0.399	0.676	4037.644	0.214	0.040	0.099	0.281	0.263	0.051	0.237	0.432	251.435	0.245	251.822	0.586	0.432
z10	6.985	0.879	0.672	474.147	0.212	0.040	0.185	0.283	2.025	0.052	1.973	0.320	251.662	0.455	253.362	4.540	0.320
z11	10.737	0.445	0.672	1404.695	0.212	0.040	0.168	0.281	0.693	0.051	0.661	0.304	251.421	0.415	251.567	1.544	0.304
z12	34.641	0.500	0.689	3974.906	0.218	0.040	0.066	0.281	0.260	0.051	0.247	0.311	251.478	0.164	251.385	0.579	0.311
z13	31.633	0.571	0.662	3207.811	0.209	0.040	0.054	0.281	0.309	0.051	0.296	0.322	251.497	0.133	251.582	0.688	0.322

Table S2. Cont.

Sample and fraction	Composition			Isotopic ratios									Dates (Mya)				
	Pb* (pg)†	Pbc (pg)‡	Th/U§	206Pb/ 204Pb¶	208Pb/ 206Pb‖	206Pb/ 238U‖	±2s %	207Pb/ 235U‖	±2s %	207Pb/ 206Pb‖	±2s %	Correlation coefficient	206Pb/238U <Th>**f	±2s absolute††	207Pb/ 235U‡‡	±2s absolute††	Correlation coefficient
z15	17.101	1.216	0.666	826.874	0.211	0.040	0.113	0.282	1.150	0.051	1.114	0.364	251.620	0.279	252.266	2.569	0.364
z16	7.036	0.607	0.735	672.915	0.232	0.040	0.115	0.281	1.386	0.051	1.363	0.240	251.577	0.284	251.759	3.090	0.240
z17	10.339	0.356	0.680	1679.481	0.215	0.040	0.064	0.282	0.574	0.051	0.565	0.195	251.796	0.159	251.968	1.282	0.195
z18	13.277	0.421	0.688	1822.853	0.218	0.040	0.055	0.282	0.512	0.051	0.501	0.238	251.738	0.135	252.339	1.143	0.238
z21	9.031	0.303	0.646	1738.759	0.204	0.040	0.071	0.283	0.543	0.051	0.529	0.252	252.199	0.175	252.671	1.214	0.252
z22	8.823	0.319	0.691	1598.787	0.218	0.040	0.078	0.281	0.578	0.051	0.565	0.225	251.502	0.193	251.742	1.288	0.225
z24	5.638	0.461	0.758	705.476	0.240	0.040	0.121	0.281	1.334	0.051	1.313	0.216	251.471	0.300	251.540	2.973	0.216
z25	10.546	0.801	0.613	785.193	0.194	0.040	0.104	0.282	1.169	0.051	1.148	0.243	251.435	0.255	252.072	2.609	0.243
z26	12.856	0.439	0.661	1704.160	0.209	0.040	0.062	0.282	0.544	0.051	0.535	0.203	251.482	0.154	252.107	1.215	0.203

Analyses highlighted in gray are not included in the weighted mean calculation.

†Total mass of radiogenic Pb.

‡Total mass of common Pb.

§Th contents calculated from radiogenic ^{208}Pb and the ^{207}Pb/^{206}Pb date of the sample, assuming concordance between U-Th and Pb systems.

¶Ratio of radiogenic Pb (including ^{208}Pb) to common Pb.

‖Measured ratio corrected for fractionation and spike contribution only.

**Measured ratios corrected for fractionation, tracer, and blank.

††Isotopic dates calculated using the decay constants λ^{238} = 1.55125E−10 and λ^{235} = 9.8485E−10 (1).

‡‡Corrected for initial Th/U disequilibrium using radiogenic 208Pb and Th/U[magma] = 3.00000.

1. Jaffey A, Flynn K, Glendenin L, Bentley W, Essling A (1971) Precision measurement of half-lives and specific activities of ^{235}U and ^{238}U. *Phys Rev C Nucl Phys* 4:1889–1906.